

APPLICATION OF AMBIENT NOISE TOMOGRAPHY IN PART OF SOUTH CHINA BASED ON SELF-DEVELOPED SEISMIC RECORDER

GUANGHUA PANG^{1,2}, PENG XUE^{1,2}, WEI WANG², JUN LIN¹ and SHENGBAO YU¹

¹ College of Instrumentation and Electrical Engineering, Jilin University, Changchun 130061, P.R. China. pghua7@163.com

² College of Electrical and Electronic engineering, Changchun University of Technology, Changchun 130021, P.R. China.

(Received December 21, 2021; revised version accepted May 10, 2022)

ABSTRACT

Pang, G.H., Xue, P., Wang, W., Lin, J. and Yu, S.B., 2022. Application of ambient noise tomography in part of South China based on self-developed seismic recorder. *Journal of Seismic Exploration*, 31: 357-373.

The broadband seismic recorder is an essential instrument for accurately determining the subsurface structure. In this paper, the velocity structure of the crust beneath the juncture area of Anhui Province, Jiangxi Province and Zhejiang Province of China was imaged using ambient seismic noise recorded by 10 broadband seismic stations equipped with self-developed three-component seismic recorder. All available three-component time series spanning the breadth of 11 months from October 2014 to August 2015 were cross-correlated to yield Empirical Green's Functions for Rayleigh and Love waves. Group-velocity dispersion curves for the Rayleigh waves and the Love waves were measured by applying the frequency-time analysis method. Then dispersion measurements were utilized to construct 2D group-velocity maps for the Rayleigh wave at 3-20 s periods and the Love wave at 7-20 s periods, respectively. Both the Rayleigh and Love wave group-velocity maps obtained show particularly slight heterogeneity in general when compared with the average velocity. Nevertheless, there exists a same remarkable and intuitive velocity-difference boundary between high velocity and low velocity in both group-velocity maps for the Rayleigh wave at 9-13 s periods and the Love wave at 15-18 s periods, which are well in accordance with horizontal shear-wave velocity structure at depth of 14-21 km derived from known Crust 1.0.

KEY WORDS: crust structure, ambient noise tomography, Rayleigh wave, Love wave.

INTRODUCTION

Broadband seismic data are essential for geophysical methods such as tomography and full wave inversion for detecting the internal structure of the Earth. The broadband seismometer such as REFTEK130 and QQ330 which are suitable for prolonged field work, is a fundamental instrument for recording continuous ambient noise. Now, the good test results of the digital broadband seismograph GEI researched and developed by Jilin University (Wu, 2013) are obtained through theoretic analysis and verification in laboratory (Wu, 2013; Liu, 2014). A field experiment deploying ten seismic stations with the GEI in part of South China was made to examine the applicability and quality of this new instrument further.

Ambient noise tomography (ANT) is a typical application method for broadband seismic data from broadband seismometers. Ambient noise is now generally believed to be a valuable source of information regarding crustal media. The Empirical Green's function (EGF) of surface waves can be derived from the cross-correlation of continuously recorded ambient seismic noise, to obtain the subsurface velocity structure (e.g., Shapiro and Campillo, 2004; Sabra et al., 2005; Shapiro et al., 2005; Yao et al., 2006). This method does not require seismic signals from natural earthquakes or active sources; instead, it uses continuous ambient seismic noise. ANT, compared with traditional seismic analysis methods, exhibits several advantages: less restrictions on the distribution of seismic sources and study regions; no limitation on the the time and place of the earthquake; more homogeneous lateral resolution; shallower depth to gain velocity structure. Furthermore, it contains comprehensive sampling medium information of different scattering paths between station pairs and is more sensitive to the changes of medium properties compared with direct wave. And the "source" (station) position is fixed and can be measured accurately, with the cost advantage incomparable.

If the method of ANT is explored and applied successfully by using the data from the GEI based on application test in the field mentioned above, from another aspect, it would implicitly illustrate that the GEI system can work stably and meet the requirements of long-term work with good performance, and that the GEI would have a promising prospect to be applied in large-scale field observation system of comprehensive seismic research.

Therefore, in this paper, we collected three-component seismograms from 10 GEI broadband stations based on the field experiment mentioned above to retrieve the group velocity tomography of both the Rayleigh wave and the Love wave through ambient noise cross-correlations. The resulting Rayleigh-wave and Love-wave group-velocity maps generally show good correlations with known velocity structure in the region studied. The test run through the outdoor experiment and successful application of ANT method based on the data recorded proved that the design of the GEI is feasible and well-performed.

DATA AND CROSS-CORRELATION CALCULATION

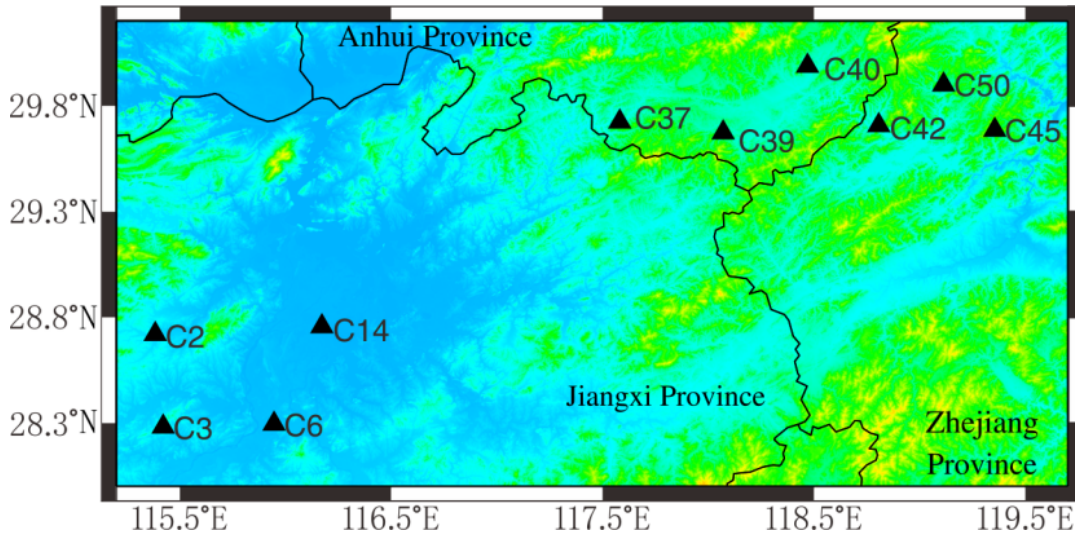


Fig. 1. Distribution of seismic stations and the background tectonic map of the area studied. With the black triangles for GEI broadband stations and the black curves for the province boundary.

Continuous data in the three components - namely the east (E), north (N), and vertical (Z) components, were recorded by 10 GEI broadband stations in South China from October 2014 to August 2015. The station locations ranged from 115.2°E to 119.7°E in longitude and from 28°N to 30.2°N in latitude, covering the juncture of Anhui Province, Jiangxi Province and Zhejiang Province of China. The distribution of the stations is illustrated in Fig. 1.

Additionally, the GEI system has been introduced in detail in the literature of Wu 2013. The performance indexes including the noise, harmonic distortion, common mode rejection ratio, and crosstalk between channels, for the self-developed GEI broadband seismic recorder have been repeatedly tested by Wu et al. (2013) and Liu et al. (2014), and the performance comparisons between the GEI and Reftek 130 are summarized and listed as below in Table 1.

Table 1. Performance indexes of self-developed GEI digital broadband seismograph and Reftek 130.

<i>Performance Index</i> Seismograph	Noise Level	Harmonic Distortion	Common Mode Rejection Ratio (CMRR)	Synchronization Accuracy	Crosstalk Suppression
REFTEK-130	1.589 μ v	-	70dB	\pm 100 μ s	-
Self-developed GEI	1.555 μ v	<-95dB	>110dB	\pm 3.2 μ s	>115dB
<i>Performance Index</i> Seismograph	Transmission Mode	Positioning Accuracy	Function Integration		
REFTEK-130	10M Ethernet	Null	Collection		
Self-developed GEI	100M Ethernet 10Mbsp WiFi	Decimeter Scale	<ul style="list-style-type: none"> •Wireless Communication •Location•Collection•Battery 		

The experiment included comparison testing of the recorded data from the GEI and the REFTEK 130. i.e. the GEI and the REFTEK 130 were simultaneously connected to the same seismometer, CMG-3ESPC, at station C40. And the three-component seismograms recorded by the GEI and Reftek 130 are graphed and compared and shows they have high consistency, respectively, which has been documented in the literature of Pang 2017. Here we show two examples about noise and seismic signal.

The ambient noise data recorded by the GEI and Reftek 130 lasts for 10 second hour from 00:00:00 to 00:00:10 on Oct 9, 2014, and are compared within the same coordinate system in the Fig. 2. The data were all recorded with a 100-Hz sampling frequency. The ambient noise in three components from the GEI are identical with those from Reftek 130.

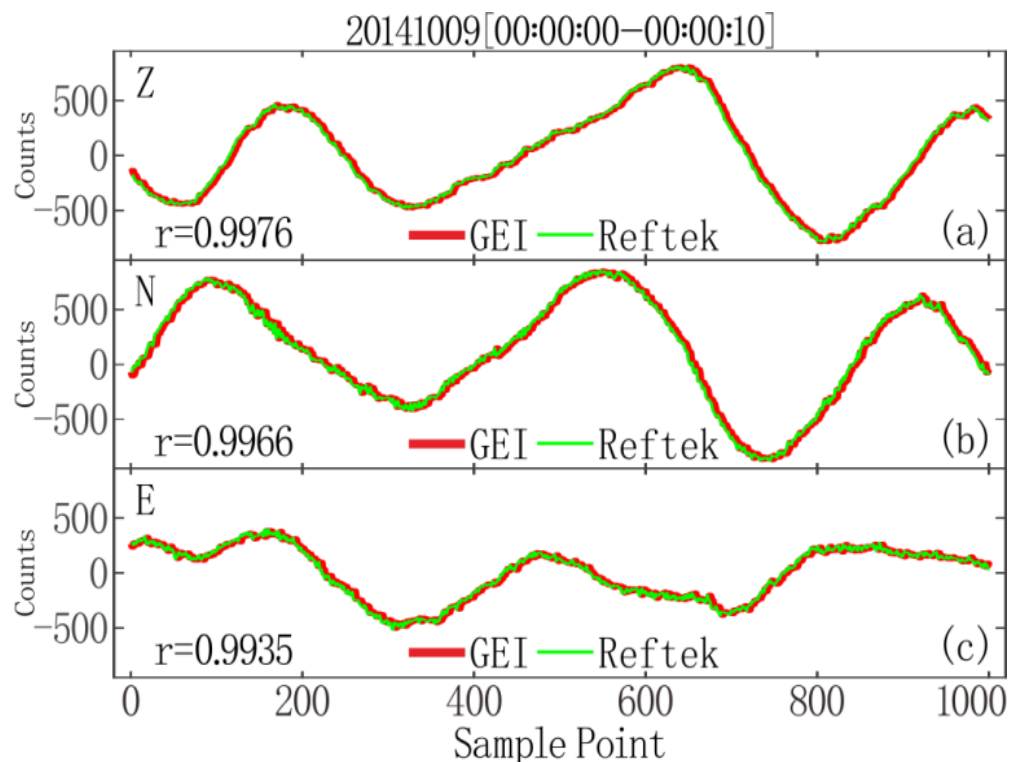


Fig. 2. 10-second time-domain waveforms in the three components of ambient noise data recorded by the GEI and Reftek 130. The 'r' represent correlation coefficient.

An earthquake with a magnitude of 6.2 and a focal depth of 50 km occurred on December 21, 2014, at 19:34:12 (Beijing Time) in Molukka Sea (126.80°E, 2.25°N). We cut the data recorded by both the GEI and Reftek 130 from 12:14:00 to 23:58:00 on December 21, 2014. The amplitudes and waveform shapes of the seismic waveform in each of the three components recorded by the GEI almost completely resemble those recorded by the Reftek 130 as shown in Fig. 3.

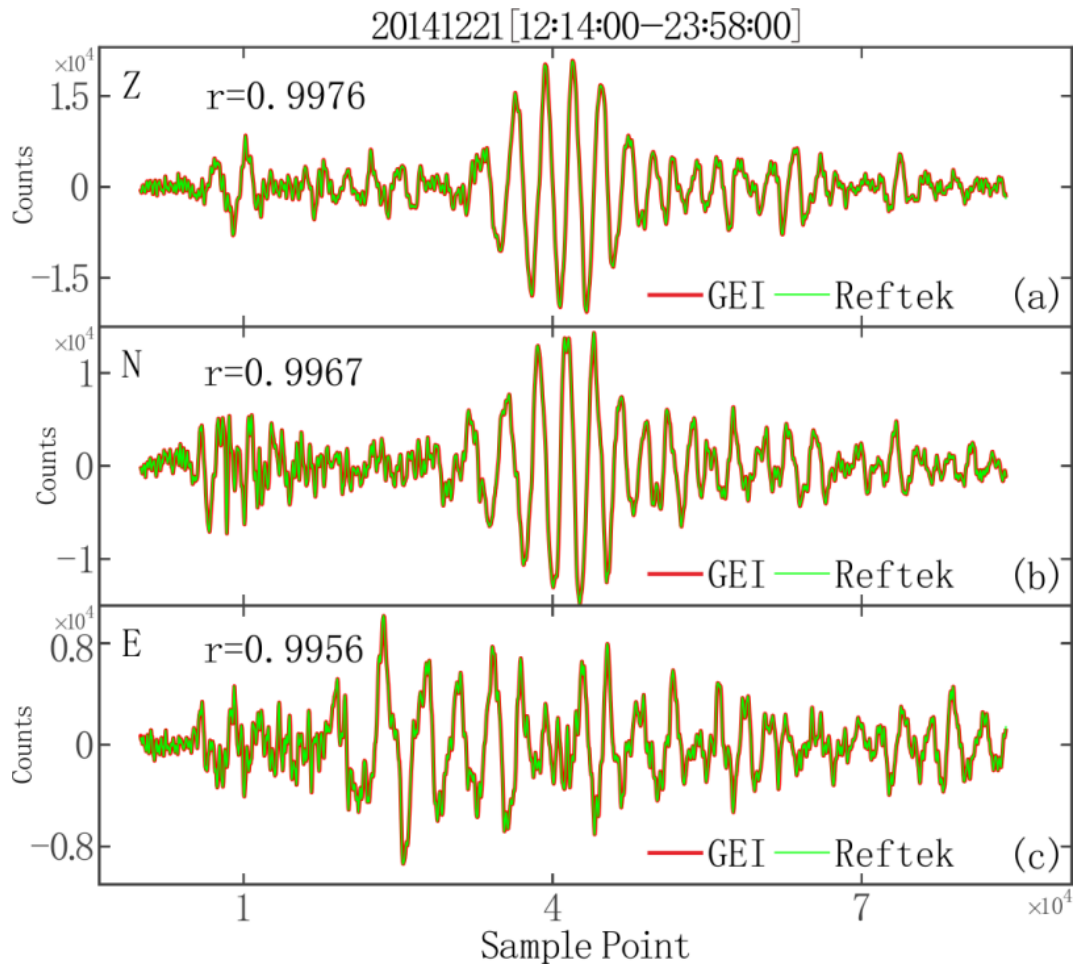


Fig. 3. The time-domain waveforms in the three components of teleseism recorded by the GEI and Reftek 130. The 'r' represent correlation coefficient.

The academic theory and practical exploration of the Ambient Noise Tomography method based on cross-correlation calculation have been researched profoundly and extensively (Campillo and Paul, 2003; Weaver and Lobkis, 2004; Weaver, 2005; Shapiro et al., 2004, 2005; Roux et al., 2005; Sabra et al., 2005; Bensen et al., 2007). The process framework of data pre-processing makes reference to previous achievement of Bensen et al. (2007). Specifically, the three-component seismic records in the daily-time series of each station were processed in order by removing the mean value, instrument response, band-pass filtering in 2.25-60 s, time-domain normalization and spectrum whitening.

After all these pre-processing steps were implemented, the component cross-correlations of the daily records (E-E, E-N, N-E, N-N, Z-Z) between each station pair were carried out and one-year of daily cross-correlations were stacked to obtain the final cross-correlations. The cross-correlations for the N-N, N-E, E-N, and E-E components were then rotated into the radial (R-R) and the transverse (T-T) components using a rotation matrix below (e.g., Lin et al., 2007).

$$\begin{pmatrix} TT \\ RR \\ TR \\ RT \end{pmatrix} = \begin{pmatrix} -\cos\theta \cos\psi & \cos\theta \sin\psi & -\sin\theta \sin\psi & \sin\theta \cos\psi \\ -\sin\theta \sin\psi & -\sin\theta \cos\psi & -\cos\theta \cos\psi & -\cos\theta \sin\psi \\ -\cos\theta \sin\psi & -\cos\theta \cos\psi & \sin\theta \cos\psi & \sin\theta \sin\psi \\ -\sin\theta \cos\psi & \sin\theta \sin\psi & \cos\theta \sin\psi & -\cos\theta \cos\psi \end{pmatrix} \times \begin{pmatrix} EE \\ EN \\ NN \\ NE \end{pmatrix}.$$

Subsequently, the positive and negative components of the cross-correlations were stacked to determine the so-called “symmetric components” for enhancing the signal-to-noise ratio (SNR).

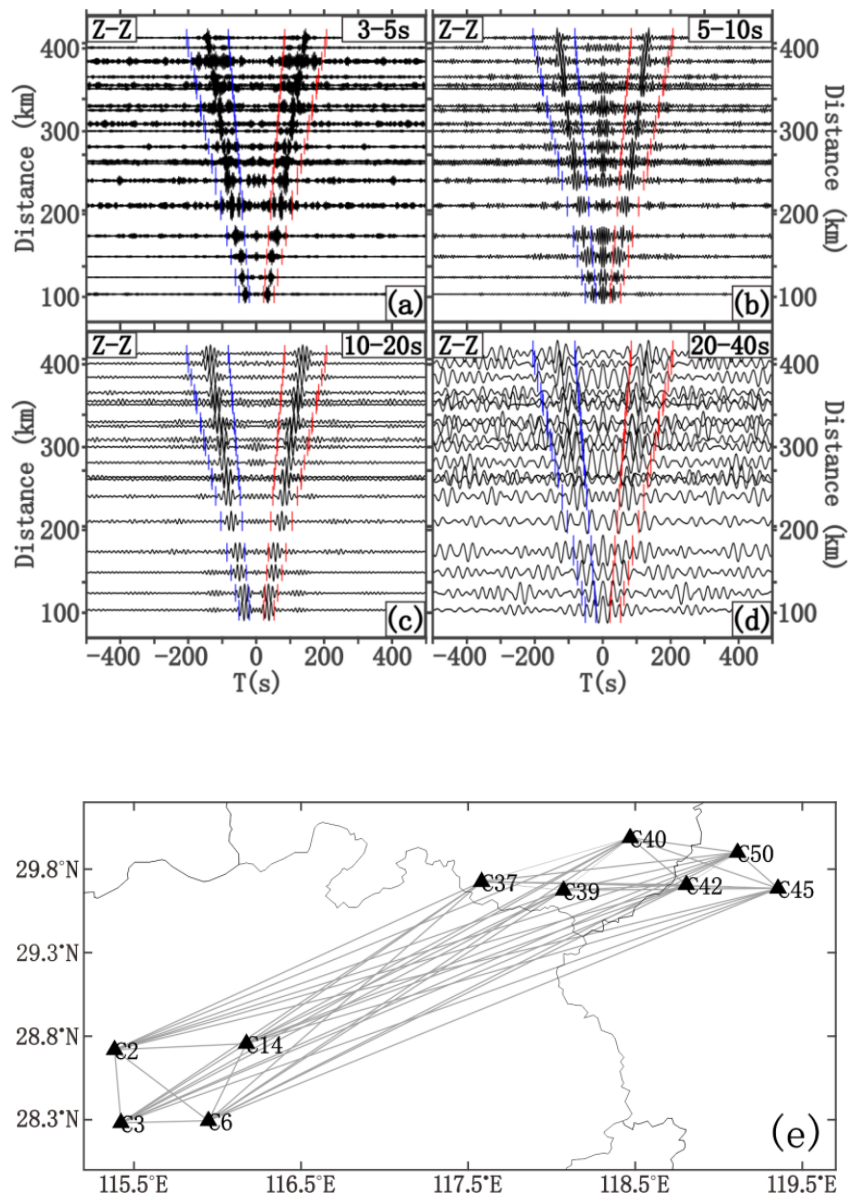


Fig. 4. Bandpass-filtered cross-correlations from vertical component in the 3-5 s(a), 5-10 s(b), 10-20 s(c) and 20-40 s(d) period ranges. (e) The corresponding ray path distribution of the cross-correlations.

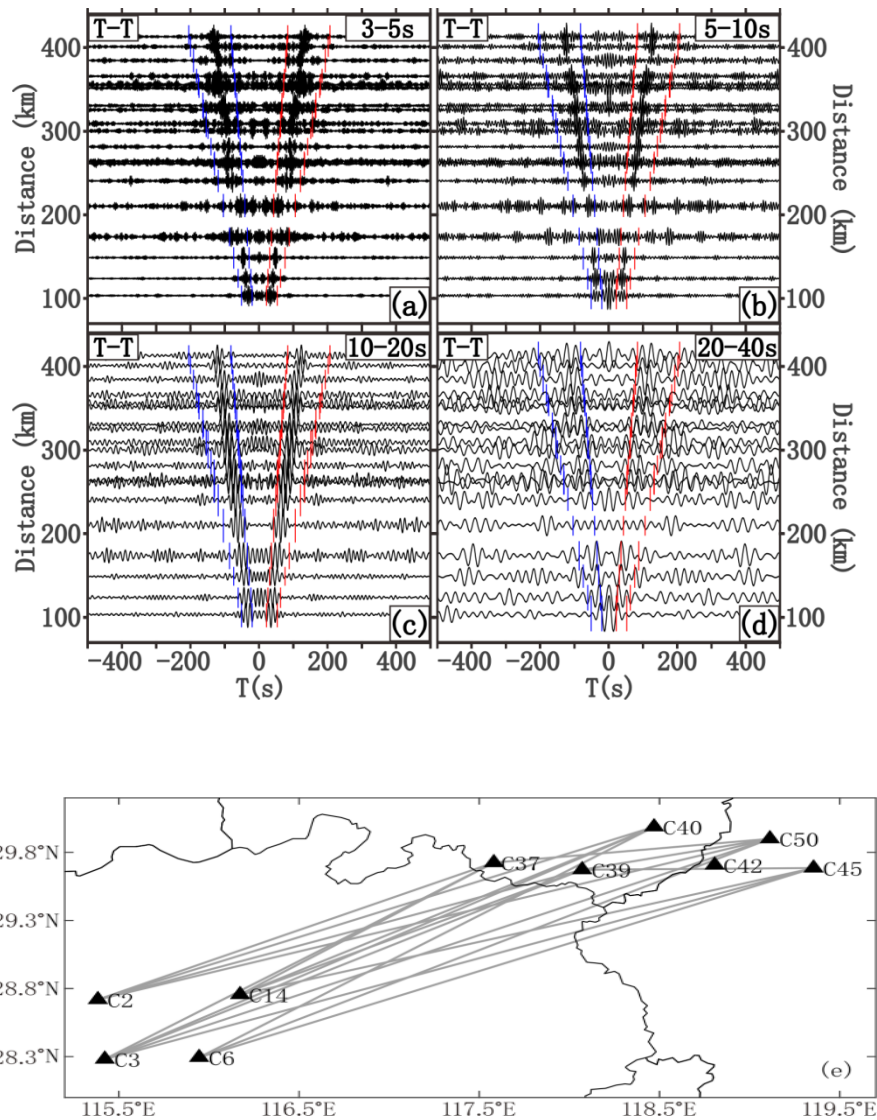


Fig. 5. Bandpass-filtered cross-correlations from transverse component in the 3-5 s(a), 5-10 s(b), 10-20 s(c) and 10-20 s(d) period ranges. (e) The corresponding ray path distribution of the cross-correlations.

Fig. 4 expresses the symmetric vertical cross-correlation signals with high SNR between the station-pairs in four narrower period bands of 3-5 s(a), 5-10 s(b), 10-20 s(c) and 20-40 s(d) and the corresponding ray path distribution(e). Both the two lines represent propagation time window of the signal with 3 km/s and 5 km/s. Fig. 5 is same to Fig. 4 except transverse cross-correlation signals. The main surface wave signals of Rayleigh wave and Love wave, namely maximum amplitudes, are both quite stable in the 3-5 s, 5-10 s and 10-20 s filtering bands. The signals are dominant in the 10-20 s, i.e., the second microseism band, and deteriorates in the longer period bands (e.g., 20-40 s). Considerable asymmetries in the amplitude of the vertical original cross-correlation between the station C3 and station C50 are typically illustrated in Fig. 6. And the two two-green lines in Fig. 6

represent the signal's time window with velocity 3 km/s and 5 km/s in positive and negative branches of the cross correlation, respectively. The dominant noise sources were thus roughly located toward the southwest of the deployment, as indicated by the red arrow in Fig. 6.

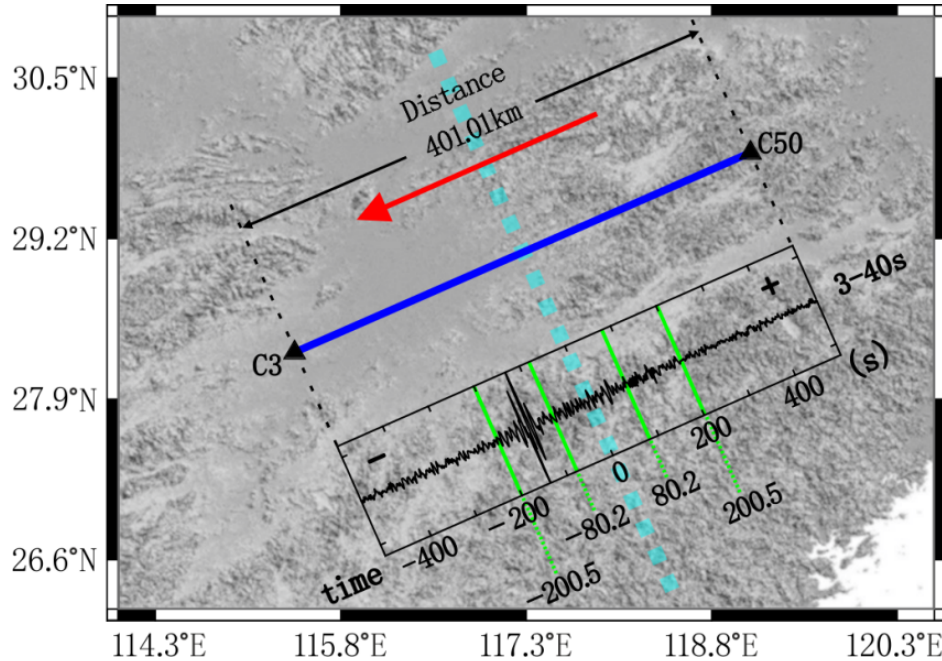


Fig. 6. The distribution of noise based on cross-correlation between station C3 and station C50.

GROUP VELOCITY-DISPERSION MEASUREMENT AND ANALYSIS

The multiple filtering technique of the time frequency analysis has proved to be an effective and fast method for analyzing the dispersion characteristics of surface waves. In this article, we measured both the Rayleigh-wave group-velocity dispersions and Love-wave group-velocity dispersions from the stacked EGF using the multiple filtering method, which can rapidly track the entire dispersion curve. Take the station pair C3-C50 for example and the steps are as follows: First of all, using Matlab to take the fast Fourier Transform for the time-domain signal of the symmetric cross-correlations $W(t)$ (e.g., Fig.7a) from the previous step, and consequently, the frequency-domain signal (i.e., frequency spectrum) $W(\omega)$ (e.g., Fig.7b) is obtained. Subsequently, the filtered frequency-domain signal $G(\omega)$ (e.g., Fig.7d) is obtained by the Gauss filtering function (e.g., Fig.7c), and the frequency-time domain function $S(\omega, t)$ (e.g., Fig.7c) is available from the $G(\omega)$ by Fourier inverse transform. The final step is to measure the maximum amplitudes $A = |S(\omega, t)|$ and the time to reach the maximum amplitude $T(\omega)$, so the group velocity is $U(\omega) = D/T(\omega)$. Therefore, the group-velocity dispersion curve is acquired from the $U(\omega) = D/T(\omega)$ with different frequencies corresponding to different velocities (e.g., Fig. 8).

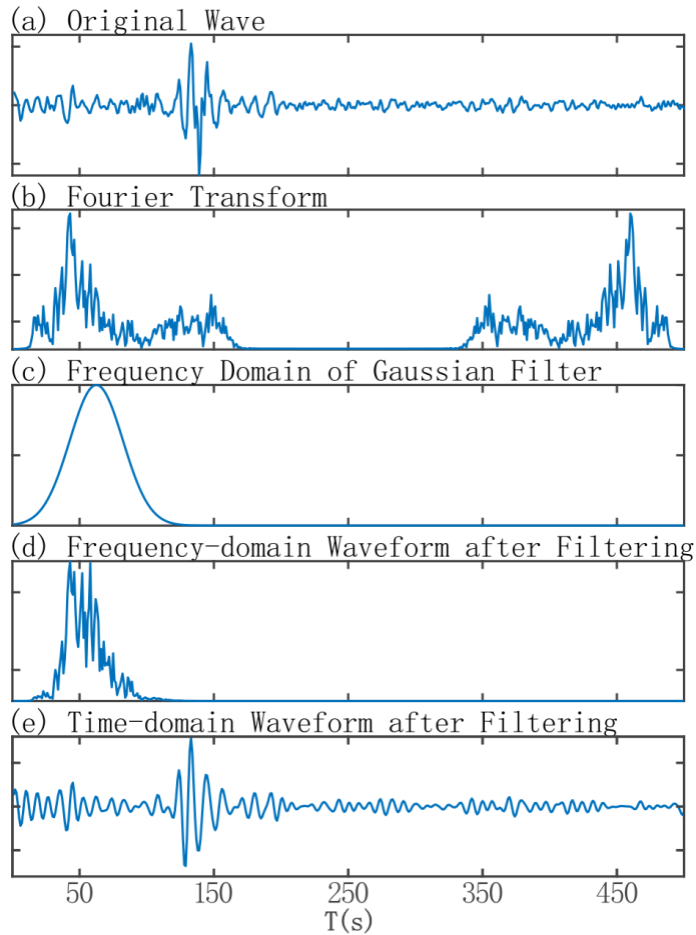


Fig. 7. The process of filtering the cross-correlation waveform by the Gaussian filtering of the center frequency 0.125HZ.

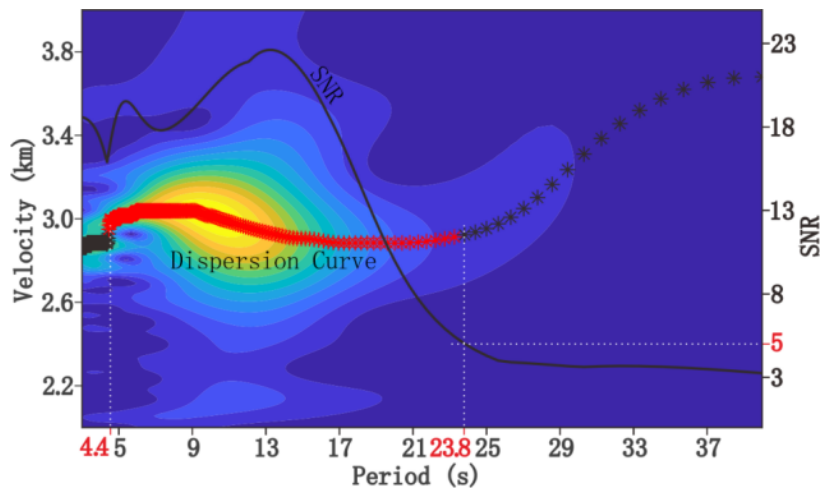


Fig. 8. Diagram of the Rayleigh wave group-velocity dispersion measurement for the C3-C50 path. All the asterisks are the automatically picked dispersion curves from the EGF at periods of 3-40 s; the black curve represents the SNR of the dispersion curve; the red asterisks indicate the extracted dispersion points with SNR values greater than 5. The distribution of seismic stations C3 and C50 and the C3-C50 path refers to Fig. 6. The original cross-correlation is given in Fig. 6.

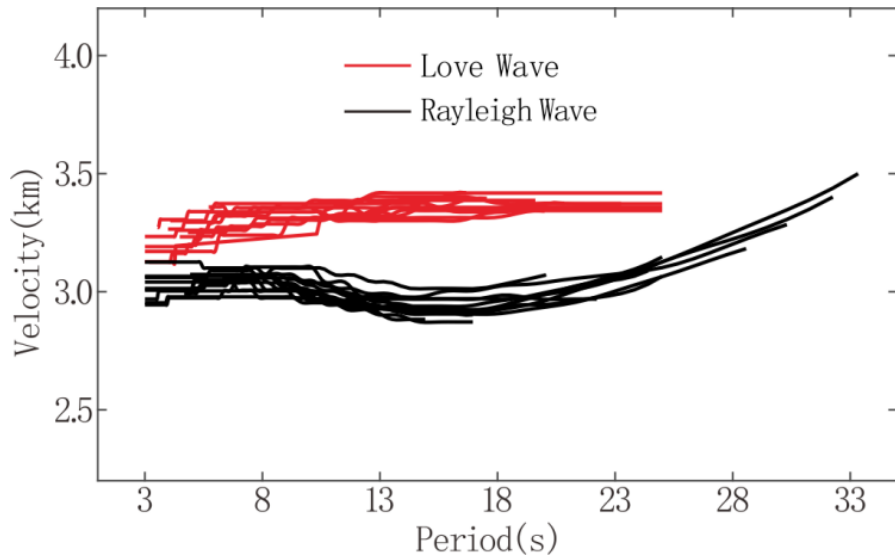


Fig. 9. All selected group-velocity dispersion curves. The black lines and red lines denote group-velocity dispersion curves of the Rayleigh waves and the Love waves, respectively.

To exclude spurious signals from interference between the two branches (Shapiro et al., 2005; Lin et al., 2007) and retain the reliable dispersion curves, three standards for selecting dispersion curves were enforced: (i) the measurements with a signal-to-noise ratio (SNR) smaller than 5; (ii) the measurements with the inter-station distance more than two wavelengths; (iii) the measurements with the reasonable shape and the morphological analysis.

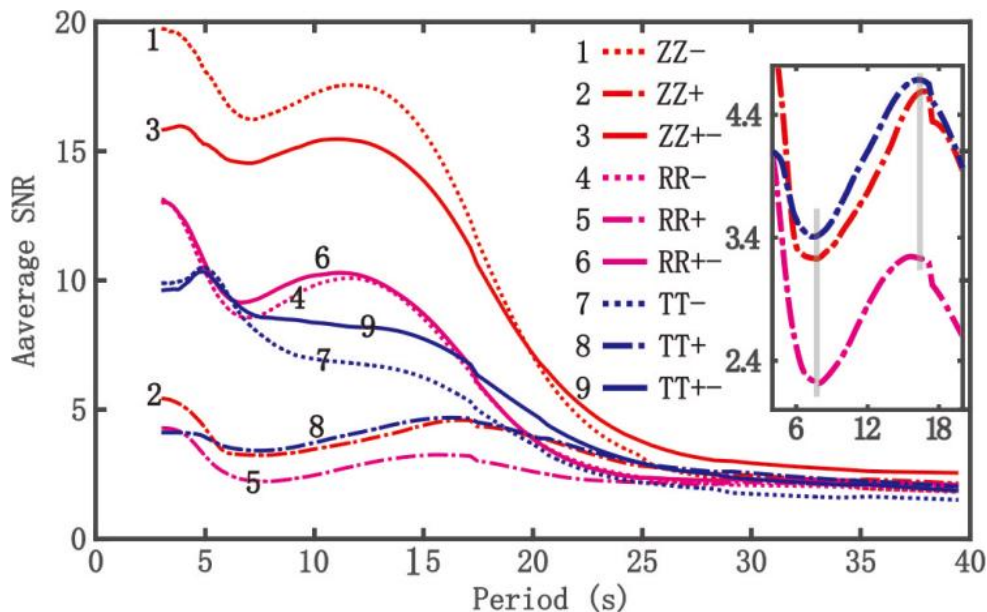


Fig. 10. The average SNRs of Rayleigh wave and Love waves cross-correlations for positive branch, negative branch, and their stack. The "ZZ-" represents the average SNRs of the negative Z-Z cross-correlations; the "ZZ+" and the "ZZ+-" are the same to "ZZ-" but for positive branch and the their stack between the negative and positive branches; "RR-", "RR+", "RR+-" and "TT-", "TT+", "TT+-" are same to "ZZ-", "ZZ+", "ZZ+-", but for R-R and T-T cross -correlations, respectively.

The average SNRs of negative component (ZZ-) and positive component (ZZ+) and their stack (ZZ+-) of Z-Z cross-correlations are detected in Fig.10. The average SNRs of ZZ- and ZZ+- decrease progressively from the periods at 3 s and 40 s with sharp slipping after 11.5s especially, and maximize at beginning period of 3 s with a bottom peak at period of 7 s and a top peak at period of 11.5 s especially. Moreover, the two low peak shapes are quiet similar, and so are the two top peak shapes. The reason needs further analysis. It is extraordinary that the average SNRs of ZZ+- is distinctly lower than those of ZZ- before period 20 s, principally contributing to the non-homogeneous poloidal distribution of the noise source. However, for the sake of gaining long-term dispersion, the cross-correlations of the ZZ+-, instead of that of the ZZ-, are extracted into dispersion. In addition, another character is that average SNRs of ZZ- , RR- and TT- have almost same shapes with same bottom peak and same top peak.

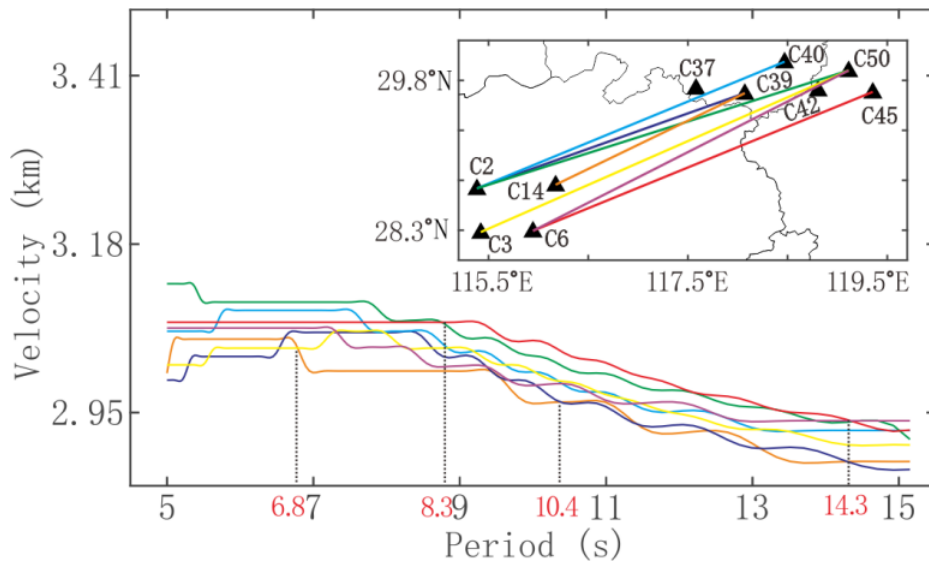


Fig. 11. Group-velocity dispersion curves of Rayleigh wave at short period band 5-15s

We performed screening results of the group-velocity dispersion curves at short period 5-15 s in Fig.11 and long period 5-25 s in Fig.12. The different colors in dispersion curves correspond to the coloured rays across different geological units. Their own morphological characteristics of the measurements across different structures distinctly reflect the differences in underground medium along the specific paths. Furthermore, in order to discuss velocity variability in the shallow crust of the study area, we focus on 5-15 s Rayleigh-wave phase-velocity dispersion curves of seven station pairs (Fig.11). All the seven dispersions with 5-15 s have a common characteristic of a gradually slow decline tendency. Besides, they also have respective peculiarity, for instance, there was the highest velocities presence along the C6-C45 at period 8.3-14.3 s and the lowest velocities presence along the C14-C39 at period 6.8-10.4 s among the other dispersions. That unveils a high average V_s structure in the upper and perhaps also middle crust beneath C6-C45 than beneath C14-C39.

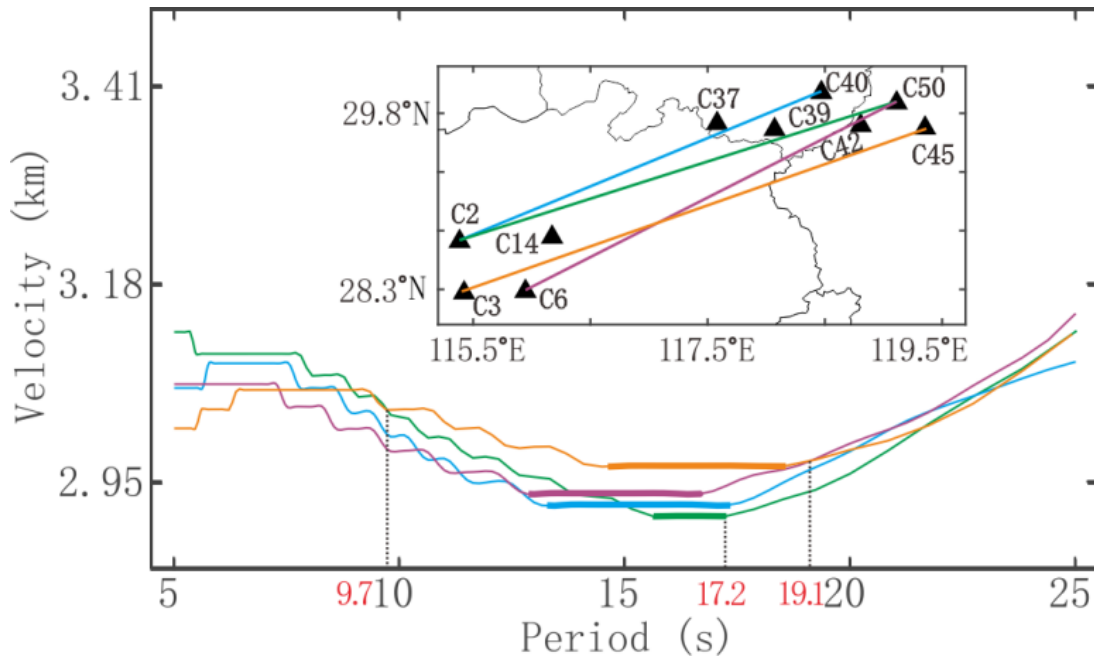


Fig. 12. Group-velocity dispersion curves of Rayleigh wave at long period band 5-25 s.

The four dispersions with 5-25 s have a certain trait in common of approaching a stable horizontal straight line individually (the thick lines given in Fig. 12) at about 13-19 s, being mutually non-coincident parallel, which hints there is a high homology in structures from middle to lower crust beneath C2-C40, C2-C50, C3-C45 and C6-C50. Nevertheless, the four dispersions with 5-25 s also have their own unique features: the much higher velocities are clearly observed between the station pair C3-C45 at period 9.7-17.2 s when compared with those of other station pairs as displayed in Fig. 12. Additionally, Fig.12 also demonstrated that the fluctuation scopes of the four dispersions at a common period are neither constant nor narrow with the period getting longer slipping beginning at 17.2s, particularly at 22 s-24 s, which implies that velocity heterogeneities in the shallow and middle crust are larger than lower crust between the station pairs C2-C40, C2-C50, C3-C45 and C6-C50 according to the general speaking of shorter periods sampling much shallower structures and longer periods sampling rather deeper structures.

CHECKERBOARD TEST

Checkerboard tests before tomography studying were conducted to validate the reliability of the tomographic results. Fig. 13k shows a theoretical velocity model with the initial slowness of alternating 1 and -1, which is discretized into a $0.5^\circ \times 0.5^\circ$ grid. The synthetic data of the group velocities were calculated according to the actual paths at each period. The resulting velocity models of Rayleigh wave are shown in Fig. 13(a,c,e,g) for the periods of 3 s, 7 s, 9 s and 15 s, and the resulting velocity models of Love wave are shown in Fig. 13(b,d,f,h) for the periods of 7 s, 11 s, 16 s and

20 s. The reconstructed velocity of images suggests that the resolving power is generally good in most parts of the area studied, but for Rayleigh wave in 3 s and Love wave in 7 s and 20 s, therefore, these imaging results in the area studied are for reference only.

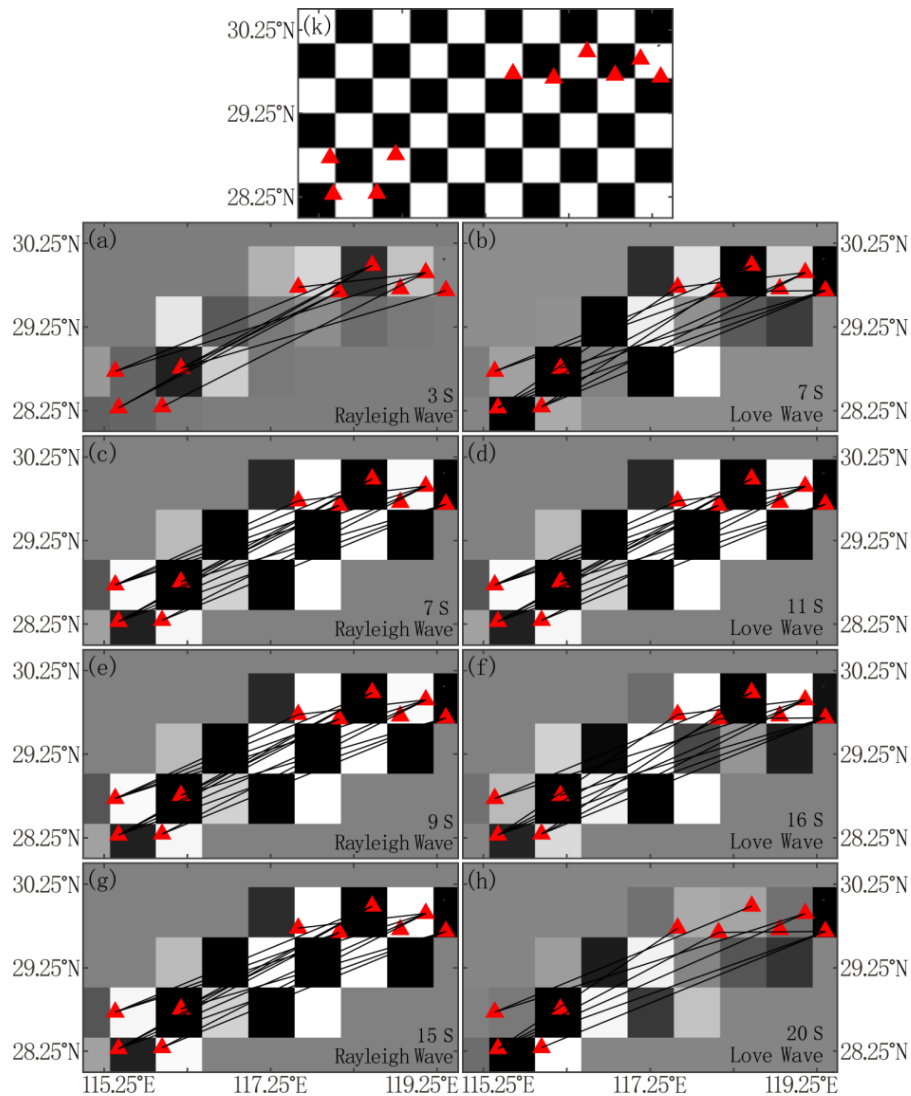


Fig. 13. The theoretical model and the results of the checkerboard test with the corresponding the path coverage. (a) the inversion result of the Rayleigh wave for $T = 3$ s path coverage; (c), (e) and (g) same as Fig. 13a but for $T = 7$ s, 9 s and 15 s, respectively; (b), (d), (f) and (h) same as Fig. 13a but for Love wave with 7 s, 11 s, 16 s and 20 s, respectively; (k) Theoretical model with the grid of 0.5° .

GROUP VELOCITY TOMOGRAPHY

We used the tomography method of Yanovskay and Ditmar (1990), which is extended from one-dimensional geophysical method of Backus-Gibert (1968) to obtain the Rayleigh-wave group-velocity variations and the love-wave group-velocity variations at different periods. This method puts forward the following three assumptions for surface wave tomography inversion.

(I) There is little difference between the actual group velocity U distribution and the initial group velocity U_0 , and the influence of deviation from the great circle path is ignored. The actual velocity disturbance value m should meet the following conditions:

$$m = (U^{-1} - U_0^{-1})/U_0^{-1} \ll 1$$

(II) When solving the velocity disturbance m relative to the initial group velocity U_0 , the disturbance values of the adjacent velocity are required to change little.

(III) The solution needs to meet the following constraints:

$$\int_s G_i(r)m(r)dr = \int_{Li} m(s)U_0^{-1}ds = \delta t_i$$

$$t_{0i} = \int_{Li} U_0^{-1}ds$$

$$\delta t_i = t_i - t_{i0}$$

Finally, the regularization law is used to minimize the following formula to obtain the group velocity distribution of Rayleigh wave or love wave at each period.

$$(d - Gm)^T (d - Gm) + a \iint |\nabla m(r)|^2 dr = \min$$

The group-velocity maps at different periods are shown in Figs. 14, 15 and 16. Both Rayleigh and Love group-velocity maps obtained show extremely weak lateral variations with ten thousandth ratio. The Rayleigh-wave and Love-wave maps at short periods [Fig.14 (a-d)] share the common feature of low velocity anomaly [dotted lines in Fig. 14 (a-d)]. Additionally, the Rayleigh-wave maps at 3 s and 7 s (Fig. 14a, c) and Love-wave maps at 11 s (Fig. 14d) exhibit broadly similar features, which can confirm each other and validate the reliability of the results simultaneously. What is more, the prominent low-velocity anomalies denoted by the black circles in Fig. 14(a-d) are corresponding to the known geological features of (Fig. 14e) the thick sediments (black circle in Fig. 14e) based on the Crust 1.0 model (Laske et al., 2015), as shown by comparing Fig. 14(a-d) with Fig. 14e. The low-velocity anomalies may be partially correlated with the elastic properties of sediments (Lin et al., 2012).

The group-velocity maps for the Rayleigh wave at 9-13 s periods (9 s example in Fig15a) and the Love wave at 15-18 s periods (16 s example in

Fig. 15b), meanwhile, appear a same noticeable and clear velocity-difference boundary between high velocity and low velocity, which was well coincident with horizontal shear-wave velocity structure at depth of 14-21 km (14 km and 21 km example in Fig. 15c and Fig. 15d, respectively) derived from known Crust 1.0 (Laske et al., 2015). Thus, the reliability of the results was confirmed. As the period gets longer, the lateral inhomogeneity of both the Rayleigh wave and the Love wave group-velocity distribution (Fig. 16) diminishes, and the imprint of the high and low velocity boundary becomes less prominent.

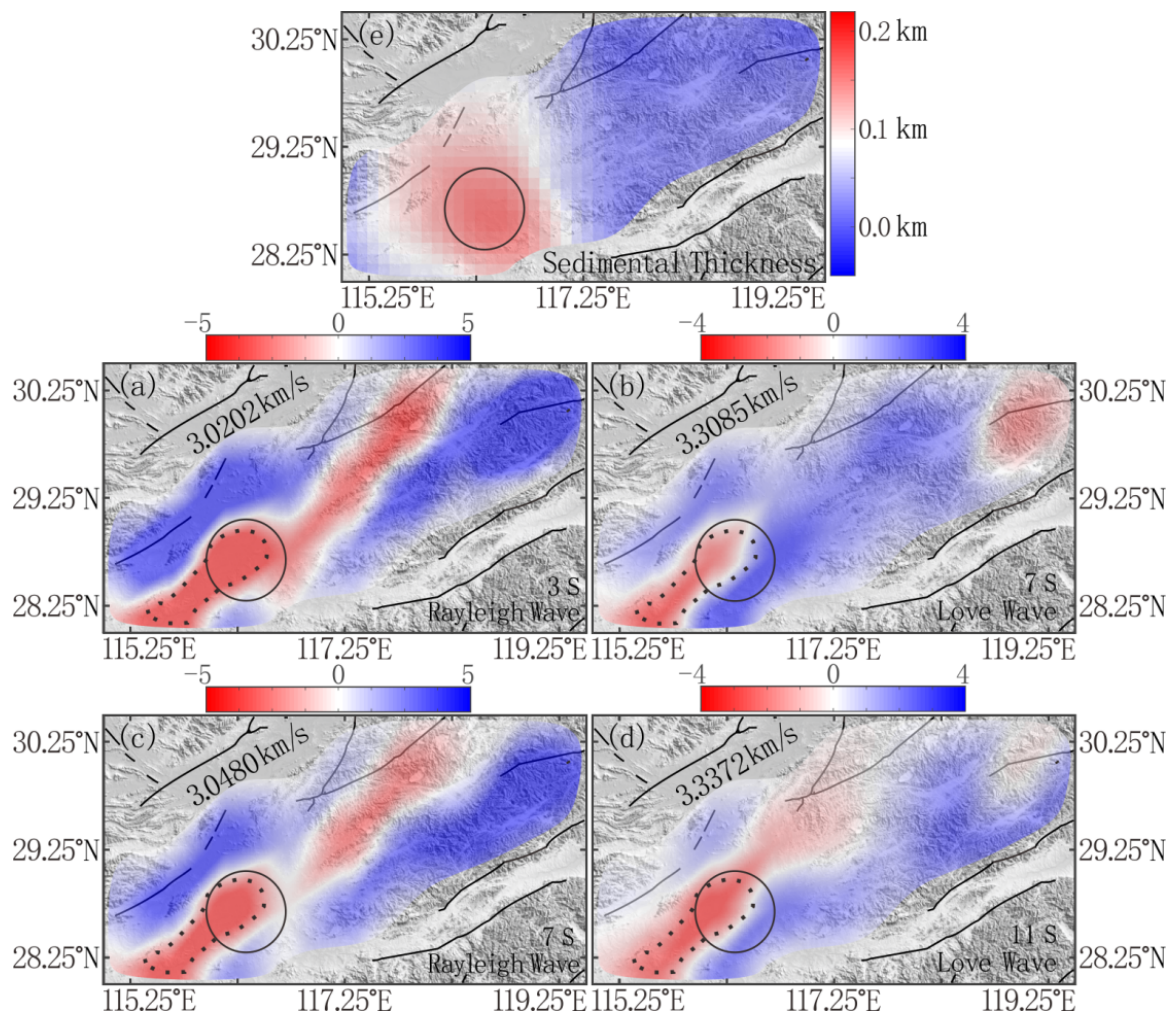


Fig. 14. Group-velocity maps at short periods and sedimentary thicknesses. The period T and average group velocity of Rayleigh wave or Love wave are labelled above each panel in Fig. 14(a)-(d). The colour bar represents the velocity anomaly in ten thousandth ratio compared with the average velocity. (The indication of the colour bar is also suited to Fig. 15 and Fig. 16).

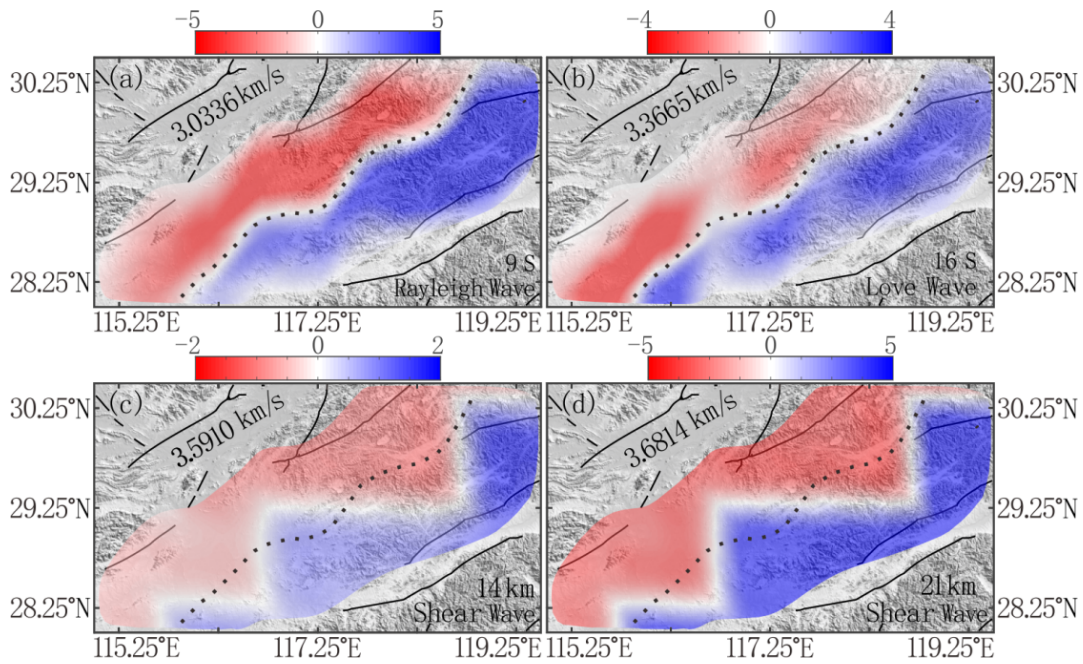


Fig. 15 Group-velocity maps at middle periods and the shear wave velocity at different depths. (a) Rayleigh-wave group-velocity maps at 9 s period; (c) is same to (a) but for love wave at 16 s; (b) Horizontal slice of the shear wave velocity structure at 14 km; (d) is same to (b) but for depth 21 km.

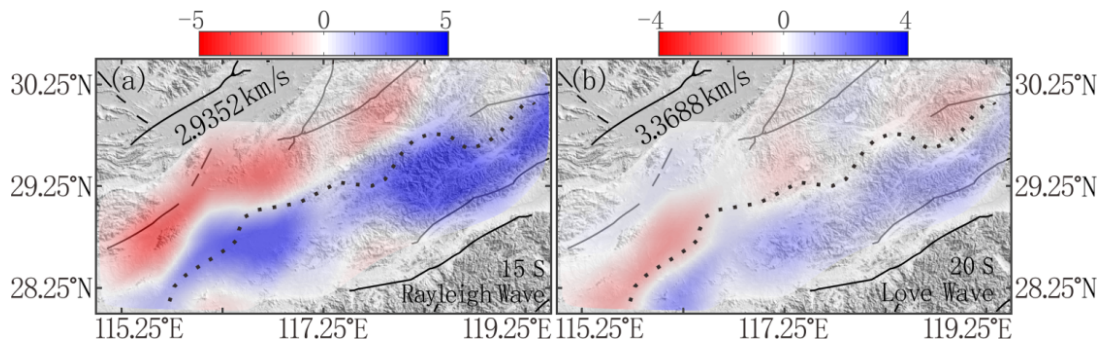


Fig.16. Group-velocity maps at long periods. (a) is Rayleigh-wave group-velocity maps at period 15 s; (b) is same to (a) but for love wave at 20 s.

CONCLUSIONS

In this paper, we conducted ambient noise tomography of juncture area of Anhui Province, Jiangxi Province and Zhejiang Province, using the data observed at the 10 broad-band stations equipped with newly-developed three-component seismic recorder GEI, and the underground structures are successfully obtained based on corresponding data processing.

The velocity anomaly of ten thousandth ratio compared with the average velocity between geological cells in the study area were observed in the Rayleigh and Love group-velocity images. The velocity distributions of Rayleigh and Love wave maps are roughly similar, and their reliability confirms each other. The images at middle period clearly

and intuitively exhibit that there exists a high and low velocity boundary, coinciding with horizontal slice of the shear-wave velocity structure based on the known Crust 1.0 model (Laske et al., 2015) extending from the middle to the lower crust.

ACKNOWLEDGEMENTS

We express our sincere thanks to all the teachers and students in the seismic group of Jilin University for their precious support and help.

REFERENCES

- Bensen, G.D., Ritzwoller, M.H., Barmin, M.P., Levshin, A.L., Lin, F., Moschetti, M.P., Shapiro, N.M. and Yang, Y., 2007. Processing seismic ambient noise data to obtain reliable broad-band surface wave dispersion measurements. *Geophys. J. Internat.*, 169: 1239-1260. doi:10.1111/j.1365-246X.2007.03374.x
- Backus, G. and Gilbert, F., 1968. The resolving power of gross earth data. *Geophys. J. Roy. Astron. Soc.*, 16: 169-205.
- Campillo, M. and Paul, A., 2003. Long-range correlations in the diffuse seismic coda. *Science*, 299: 547-549.
- Herrmann, R.B. and Ammon, C.J., 2004. Surface waves, receiver functions and crustal structure. *Computer Programmes in Seismology, Version 3.30*, St. Louis University. <http://www.eas.slu.edu/People/RBHerrmann/CPS330.html>.
- Laske, G., Masters, G., Ma, Z. and Pasyanos, M.E., 2015. Up on CRUST1.0: A 1-degree global model of the earth's crust. *Geophys. Res. Abstr.*, 15: 2658.
- Liu, T.T., 2014. Research on testing and application methods of broadband seismographys. M.Sc. thesis, Jilin University, Jilin.
- Lin, F.C., Morgan, P.M. and Michael, H.R., 2007. Surface wave tomography of the western United States from ambient seismic noise: Rayleigh and Love wave phase velocity maps. *Geophys. J. Internat.*, 173: 281-298. doi: 10.1111/j.1365-246X.2008.03720.
- Pang, G.H., 2017. Broadband Seismic Ambient Noise Tomography in Typical Regions. Ph.D. thesis, (in Chinese). Jilin University, Jilin.
- Roux, P., Sabra, K.G. and Kuperman, W.A. and Roux, A., 2005. Ambient noise cross-correlation in free space: theoretical approach. *J. Acoust. Soc. Am.*, 117: 79-84.
- Shapiro, N.M. and Campillo, M., 2004. Emergence of broadband Rayleigh waves from correlations of the ambient seismic noise. *Geophys. Res. Lett.*, 31(7): L07614. doi:10.1029/2004GL019419.
- Shapiro, N.M., Campillo, M., Stehly, L. and Ritzwoller, M.H., 2005. High-resolution surface-wave tomography from ambient seismic noise. *Science*, 307: 1615-1618.
- Sabra, K.G., Gerstoft, P., Roux, P. and Kuperman, W., 2005. Extracting time-domain Greens function estimates from ambient seismic noise. *Geophys. Res. Lett.*, 32: L03310. doi:10.1029/2004GL021862.
- Weaver, R.L. and Lobkis, O.I., 2004. Diffuse fields in open systems and the emergence of the Green's function correlation in free space: theoretical approach. *J. Acoust. Soc. Am.*, 116: 2731-2734.
- Weaver, R.L., 2005. Information from seismic noise. *Science*, 307: 1568-1569.
- Wu, H.C., 2013. Prototype Development of broadband earthquake recorder with WiFi wireless monitoring function. M.Sc. thesis, Jilin University, Jilin.
- Yao, H.J., van der Hilst, R.D. and de Hoop, M.V., 2006. Surface-wave array tomography in SE Tibet from ambient seismic noise and two-station analysis - I. Phase velocity maps. *Geophys. J. Internat.*, 166: 732-744.
- Yanovskaya, T.B. and Ditmar, P.G., 1990. Smoothness criteria in surface wave tomography. *Geophys. J. Internat.*, 102: 63-72.